Acta Technica *63* No. 4B/2018, 1–22

Survey stability of the ZVS phase-shifted full-bridge DC/DC converter with soft switching[1]

Morteza Bazghandi[1], Ali Bozorgmehr[2]

Abstract. This paper presents a new soft-switched, current driven full-bridge converter. A simple snubber is used in order to get ZVS for all the main switches. The soft-switching realization is independent of the load. The snubber is placed in parallel with the bridge. All the resonant circuit energy is recycled by the load in each half cycle. No additional current stresses appear on the main switches. A design-oriented steady-state analysis leads to the expressions of the dc voltage conversion ratio and ZVS analytical conditions, allowing for a trade-off design of the resonant inductor. A prototype has been built with a high energy transfer efficiency. Also this paper presents an in-depth critical discussion and derivation of a detailed small-signal analysis of the phase shifted full-bridge (PSFB) converter. Circuit parasitics, resonant inductance, and transformer turns ratio have all been taken into account in the evaluation of this topology's open-loop control-to output, line-to-output, and load-to-output transfer functions. Accordingly, the significant impact of losses and resonant inductance on the converter's transfer functions is highlighted. The enhanced dynamic model proposed in this paper enables the correct design of the converter compensator, including the effect of parasitics on the dynamic behavior of the PSFB converter.

Key words. Dynamic modeling, phase-shifted full-bridge (PSFB), signal analysis, zero voltage switching, DC/DC conversion.

1. Introduction

Pulse width-modulated current-driven full-bridge (FB) converters have been popularly used for applications requiring a high voltage supply system.

In order to maximize the power density of the converters, operation at high switching frequencies is chosen. For achieving low switching losses in a power converter design, soft-switching technique is necessary. For voltage driven full-bridge converters, the primary-side switches can operate under a zero voltage condition by

[1]Shahrood University of Technology, Iran; e-mail: bazghandimorteza@yahoo.com

[2]Nanotechnology & Quantum Computing Laboratory, Shahid Beheshti University, Iran; e-mail: a_bozorgmehr@sbu.ac.ir

using the phase shift control strategy [1–2]. Many studies are also devoted to zero current switched (ZCS) [3] solutions for DC/DC converters. The voltage driven full-bridge converters are suitable for low voltage applications. However, for high voltage and high power applications, boost-type input full-bridge converters are necessary.

ZVS PWM in [4] is formed by a diode, a resonant capacitor and a resistor. Its disadvantage is that during the resonant process when the resistor absorbs the resonant energy in the loop, some part of the resonant energy is thus wasted as heat, requiring a larger heat sink. In [5] ZVS is lost under light load. the active resonant cell using a pair of coupled inductors is placed in parallel with the switches bridge. The resonant current keeps flowing through the snubber during the whole free-wheeling stage, much circulating energy is lost during the process. Although there is some improvement in efficiency, the losses in the dissipative snubber limit the gain in the efficiency. In [6] and [7] active clamped snubber formed by an auxiliary switch and a resonant capacitor is proposed. The energy stored in the resonant capacitor has to be enough to discharge the leakage inductance, implying that ZVS is lost at large input current. The leakage inductance of the transformer is used to form the resonant circuit, causing an additional current stress which is much larger than I_{in} on the main switches.

A method commonly used for PWM converter dynamic model small-signal modeling is the state space averaging (SSA) technique [8]. However, no useful SSA-based dynamic modeling can be found to the PSFB because, when applied to the PSFB converter, the resulting matrices are very complex after considering the all of the operation intervals and resonant transitions.

The first PWM-switch-based [9] small-signal analysis to PSFB is presented in [10], [11], where the converter ac model is obtained as a modified version of the buck converter PWM switch model. This approach is based on a simplified analysis of the effects resulting in the duty-cycle modulation due to the change in input voltage and filter inductor current. However, this model does not consider the impact of the converter losses and, as a consequence, it does not take into account the converter efficiency. The result is a relatively simple small signal model for the PSFB converter, based on several idealistic assumptions, including zero equivalent series resistance (ESR) for the output capacitor and unity transformer turns ratio equal to 1. In [12] A further small-signal analysis of the PSFB converter has been suggested. The proposed small-signal analysis uses an unconventional averaging technique based on discrete sampled data equations. In order to exploit the benefits of the PSFB topology, considering the evolution of both the industrial applications and semiconductor technological progresses of the past decade, it is fundamentally important to revise and improve the PSFB converter dynamic model and investigate the correlations existing between the efficiency and dynamic response. Due to the lack of new enhanced PSFB small-signal models, many recent papers refer to the simplified model which is no longer adequate for modern applications of the converter [13].

In this paper, a new critical and detailed discussion of the small-signal analysis of the PSFB converter is presented and an enhanced small-signal model is derived. The proposed small signal model includes thus far neglected and yet significant factors as

well as parameters necessary for real-life practical design. Therefore, a more realistic and accurate dynamic analysis of PSFB converter with respect to previous models has been carried out. Second, this new model also allows the joint investigation of the influence of the transformer characteristics and the efficiency on the dynamic behavior of the converter. In particular, on one hand achieving SS depends on the value of the resonant inductance [14].

2. Principle of operation

The proposed current-driven FB converter is shown in Fig. 1. It is formed by a front-stage converter composed by switches S1–S4, and an output-stage rectifier composed by Dr1–Dr4. The two stages are connected by a transformer T with the turns ratio $1 : n$. The input current is supplied by a filter inductor L and Co is the output capacitor [13]–[16]. A snubber is connected across the input of the bridge to offer a zero voltage witching condition for the main switches S1–S4. The snubber is formed by a single resonant inductor Lr, an auxiliary switch Sa, an auxiliary transformer with the turns ratio 1: m, and a secondary clamping diode Da. Fig. 2 shows the theoretical switching waveforms of the proposed converter.

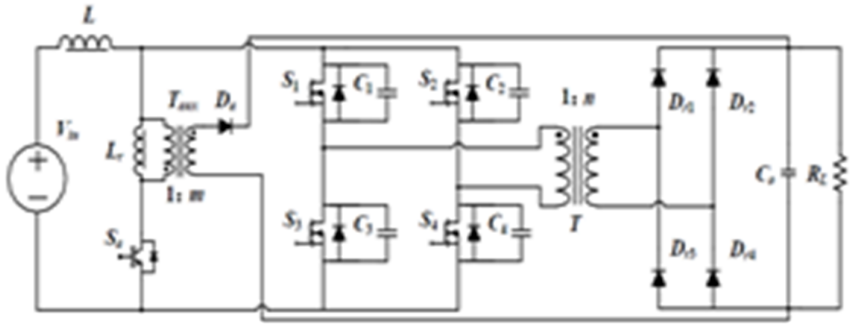

Fig. 1. Proposed ZVS FB converter

To simplify the analysis of the steady-state circuit operation, the following assumptions are made:

1) Input inductor L is large enough to keep the input current constant.

2) Output capacitor Co is large to maintain constant output voltage across [16].

3) All components including devices and transformers are ideal.

Mode 0 [$t < t_0$]: The converter operates in a freewheeling stage. Sa is turned-off and all rectifier diodes are reversed-biased. Main switches S1–S4 are turned-on and the input current flows through all these devices so that each switch carries half of the input current ideally. Accordingly

$$v_{s1}(t_0) = v_{s2}(t_0) = v_{s3}(t_0) = v_{s4}(t_0) = 0\,, \tag{1}$$

$$v_{pr1}(t_0) = v_{sec}(t_0) = v_{sa}(t_0) = 0\,, \tag{2}$$

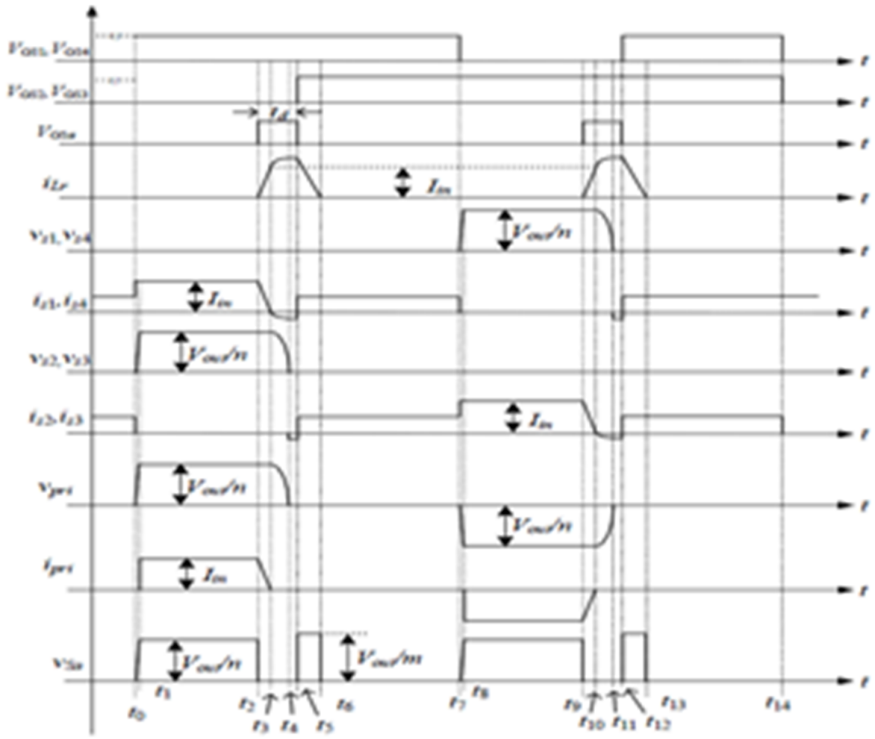

Fig. 2. Key waveforms of the converter

$$i_{s1}(t_0) = i_{s2}(t_0) = i_{s3}(t_0) = i_{s4}(t_0) = \frac{I_{in}}{2}\,, \tag{3}$$

$$i_{lr}(t_0) = 0\,. \tag{4}$$

Here, v_{s1}–v_{s4} are the voltages across the main switch S1–S4, respectively, v_{sa} is the voltage across the auxiliary switches Sa, v_{pr1} is the primary side voltage across the transformer and v_{sec} is the secondary side voltage across. Symbols i_{s1}–i_{s4} denote the currents of the main switches S1–S4, respectively, and i_{lr} is the resonant inductor current [14].

Mode 1 $t_0 \le t < t_1$]: At t_0, a new switching cycle starts with S2, S3 turning off. All input current is used to charge the capacitors C2 and C3, also all rectifier diodes are reversed-biased, meaning that rectifier circuit still operates in a freewheeling stage. The voltages of C2 and C3 increase linearly from zero. Thus, the S2 and S3 are turned off with ZVS. It can be shown that

$$v_{s2}(t) = v_{s3}(t) = v_{sa}(t) = v_{pri}(t) = \frac{I_{in}}{2C(t - t_0)}\,, \tag{5}$$

where C is the capacitance of C2 and C3. This mode ends at t_1, when the primary

voltage of the transformer reaches the reflected output voltage V_{out}/n. The energy begins transfer to the secondary side through transformer and rectifier diodes Dr_1 and Dr_2 become conducting. There holds

$$t_{01} = t_1 - t_0 = \frac{2CV_{\text{out}}}{nI_{\text{in}}}\,. \tag{6}$$

Mode 2 $t_1 \leq t < t_2$]: During this stage, the converter transfers energy to the load constantly. Now

$$v_{\text{s2}}(t) = v_{\text{s3}}(t) = v_{\text{sa}}(t) = v_{\text{pri}}(t) = \frac{V_{\text{out}}}{n}\,, \tag{7}$$

$$v_{\text{sec}}(t) = V_{\text{out}}\,, \tag{8}$$

$$i_{\text{s1}}(t) = i_{\text{s4}}(t) = i_{\text{pri}}(t) = I_{\text{in}}\,. \tag{9}$$

This mode ends at t_2 when Sa turns on to initiate the end of energy transfer [15].

Mode 3 [$t_2 \leq t < t_3$]: Due to the resonant inductor Lr, Sa can be turned on by zero current. The resonant inductor Lr begins charging linearly with the reflected output voltage V_{out}/n. The current in the snubber increases while the currents through S1 and S4 decrease, thus

$$i_{\text{Lr}}(t) = \frac{V_{\text{out}}(t - t_1)}{nL_{\text{r}}}\,, \tag{10}$$

$$i_{\text{s1}}(t) = i_{\text{s4}}(t) = i_{\text{pri}}(t) = I_{\text{in}} - \frac{V_{\text{out}}(t - t_2)}{nL_{\text{r}}}\,. \tag{11}$$

At t_3, the resonant inductor current reaches input current I_{in}. No current flows through the main transformer, and the rectifier diodes Dr1 and Dr2 turn off naturally with zero current switching. Time interval of this mode can be calculated as

$$t_{23} = \frac{nL_{\text{r}}I_{\text{in}}}{V_{\text{out}}}\,. \tag{12}$$

Mode 4 [$t_3 \leq t < t_4$]: Because of the existence of C2 and C3, a resonance path is formed by Lr, C2 and C3. Thus

$$i_{\text{Lr}}(t) = I_{\text{in}} + \frac{V_{\text{out}}\sin(t - t_3)}{nZ}\,, \tag{13}$$

$$v_{\text{C2}}(t) = v_{\text{C3}}(t) = \frac{V_{\text{out}}\cos(t - t_3)}{nZ}\,, \tag{14}$$

where $Z = \sqrt{\frac{L_{\text{r}}}{2C}}$ and $\omega = 1/\sqrt{2L_{\text{r}}C}$.

At the end of Mode 4, the resonant capacitor voltages v_{C2} and v_{C3} reach zero.

The process is independent of the load value, thus

$$t_{34} = \frac{\pi}{2\omega}\,. \tag{15}$$

Mode 5 [$t_4 \leq t < t_5$]: At t_4, the body diodes of S2 and S3 begin conducting and the switch currents are negative values. There holds

$$i_{\mathrm{Lr}}(t) = I_{\mathrm{in}} + \frac{V_{\mathrm{out}}}{nZ}\,, \tag{16}$$

$$i_{\mathrm{s1}}(t_4) = i_{\mathrm{s2}}(t_4) = i_{\mathrm{s3}}(t_4) = i_{\mathrm{s4}}(t_4) = -\frac{V_{\mathrm{out}}}{2nZ}\,. \tag{17}$$

The main switches S2 and S3 turn on with ZVS at t_5. Meanwhile, to avoid circulating energy losses in the loop formed with resonant inductor Lr and the main switches, auxiliary switch Sa should be turned off [16].

Mode 6 [$t_5 \leq t < t_6$]: After the auxiliary switch Sa turning off, the current in the in the main switches return to $I_{\mathrm{in}}/2$. The primary diode Da begins conducting and resonant inductor discharges to the load by the reflected output voltage V_{out}/m. Now

$$i_{\mathrm{Lr}}(t) = I_{\mathrm{in}} + \frac{V_{\mathrm{out}}}{2nZ} - \frac{V_{\mathrm{out}}(t-t_5)}{mL_{\mathrm{r}}}\,, \tag{18}$$

$$v_{\mathrm{Sa}} \frac{V_{\mathrm{out}}}{m}\,. \tag{19}$$

All resonant energy stored in inductor Lr is transferred to the load and

$$t_{56} = \frac{mL_{\mathrm{r}}I_{\mathrm{in}}}{2V_{\mathrm{out}}} + \frac{m}{2n\omega}\,. \tag{20}$$

Mode 7 [$t_6 \leq t < t_7$]: After t_6, v_{pri} and v_{sec} remain at zero. The operation states of the converter can be expressed by equations (1)–(4). The converter works in a freewheeling stage. At the time t_7, the converter goes into the next half of the switching cycle [16].

3. Steady-state analysis

3.1. ZVS Conditions

To achieve a nice zero voltage turn-on for each of the main switches, specific requirements should be satisfied [17]. Thus, t_d can be defined as the time interval between t_2 and t_4. Based on equations (12) and (15), t_d should fulfill the criteria

$$t_d \geq \frac{nL_{\mathrm{r}}I_{\mathrm{in}}}{V_{\mathrm{out}}} + \frac{\pi}{2\omega}\,. \tag{21}$$

3.2. DC voltage conversion ratio

The energy flow of the proposed converter is similar to a basic boost converter

$$DT_{\mathrm{s}} = t_{56} + t_{67} + \cdots + t_{13\sim14}\,, \tag{22}$$

where D is the duty cycle of the PWM.

The power converter energy balance is represented as

$$\int_{t_5}^{t_{14}} |t|t_{14} V_{\mathrm{out}}\,\mathrm{d}t = DT_{\mathrm{s}} V_{\mathrm{in}} I_{\mathrm{in}}\,, \tag{23}$$

$$\int_{t_5}^{t_{14}} |(t)|\,\mathrm{d}t = 2\int_{t_4}^{t_5} |i_{\mathrm{Lr}}(t)|/n\,\mathrm{d}t + \int_{t_1}^{t_3} |i_{\mathrm{pri}}(t)|/m\,\mathrm{d}t\,, \tag{24}$$

$$2\int_{t_4}^{t_5} |i_{\mathrm{Lr}}(t)|/n\,\mathrm{d}t = (I_{\mathrm{in}}/m + V_{\mathrm{out}}/(2mnZ))(mL_{\mathrm{r}} I_{\mathrm{in}}/(2V_{\mathrm{out}}) + m/(2n\omega))\,, \tag{25}$$

$$\int_{t_1}^{t_3} |i_{\mathrm{pri}}(t)|/m\,\mathrm{d}t = L_{\mathrm{r}} I_{\mathrm{in}}^2/(2V_{\mathrm{out}} t_2/n)\,. \tag{26}$$

By inserting the formulas (22) and (24)–(26) into (23), we obtain the DC gain M in the form

$$M = \frac{1}{\frac{1}{nDT_{\mathrm{s}}}\left(\frac{t_{12}}{V_{\mathrm{out}}} + \frac{C}{2nI_{\mathrm{in}}}\right) + \frac{1}{2DT_{\mathrm{s}}V_{\mathrm{out}}}\left(\frac{2l_{\mathrm{r}}I_{\mathrm{in}}}{V_{\mathrm{out}}} + \frac{L_{\mathrm{r}}}{2nZ} + \frac{1}{nw}\right)}\,. \tag{27}$$

4. Design considerations

4.1. Design specifications

The main parameters of the proposed ZVS full bridge converter are shown in Table 1.

Table 1. Design specifications of the prototype

Item	Values	Units	Remarks
$I_{\text{in,min}}$	3	A	minimum input current
$I_{\text{in,max}}$	10	A	maximum input current
ΔI_{in}	12	%	output current ripple
V_{in}	200	V	input voltage
V_{out}	200	V	output voltage
ΔV_{out}	8	%	output voltage ripple
f	100	kHz	switching frequency
D	0.75		designed duty cycle

4.2. Design of the resonant inductor value L_{r} and transformer turns ratio n

The minimum value of L_{r} is calculated with the limitation of resonant current peak flowing through the snubber. To avoid excessive conduction losses in the snubber, i_{Lr} should be limited to 1.5 times of the input current. Thus

$$L_{\text{r}} \geq \frac{nL_{\text{r}}I_{\text{in}}}{V\text{out}} + \frac{\pi}{2\omega}\,. \tag{28}$$

To achieve a short t_{23} and limit resonant peak current in a reasonable value, L_{r} is chosen 2µH and the turns ratio $n = 5$. Accordingly, $t_{23}3 = 50\,\text{ns}$ under full-load condition according to (12).

4.3. Design of turns ratio of the auxiliary transformer

The auxiliary transformer is designed according to the voltage stress on the auxiliary switch in mode 6. Given by equation (19), a voltage stress V_{out}/m is added across Sa. To avoid a high voltage stress in the auxiliary switch, m is chosen as equal to n.

5. Simplified PSFB small-signal models

In this section, the fundamental limitations of simplified dynamic models presented so far in the literature are highlighted and a preliminary introduction to the main parameters in the dynamic modeling of converter is given. In Fig. 3, left part, the PSFB schematic circuit is given and in Fig. 3, right part, the converter waveforms of voltage and current of primary side and the voltage and current of secondary side are shown. The finite slope of the primary side current I_{P} depends on the leakage inductance L_{leak}. The slope reduces the duty cycle of the secondary-side voltage, with a detrimental impact on the dynamic characteristics of the converter [13].

Small-signal properties are quite different, because of the converter's phase-shift operation and the presence of the transformer leakage inductance, which jointly represent the root cause of the "lost duty" phenomenon [13]. Leakage inductance

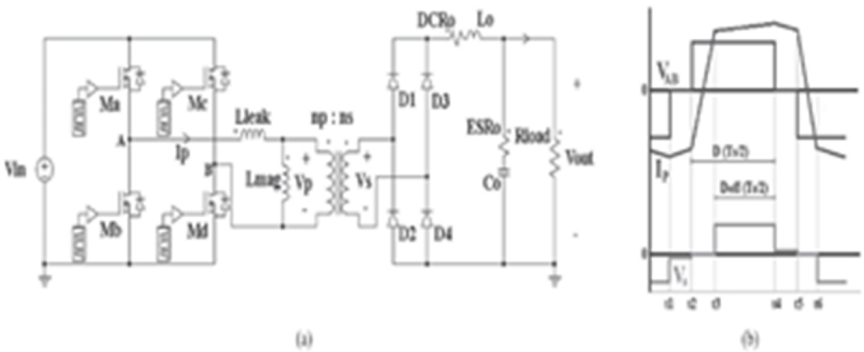

Fig. 3. Left–PSFB schematic circuit, right–main circuit waveforms

provides a first contribution for resonant inductance. In order to achieve SS in a PSFB converter, the leakage inductance alone may not be sufficient, and additional external inductor is added to primary current path [14] to achieve the desired resonant inductance. However, a resonant inductance that is too large would result in longer transition times, higher value of lost duty, and reduced dynamic range of the converter [19]. Detailed and complete description of the secondary voltage duty-cycle is included in [13], where (29) for secondary voltage effective duty-cycle is given as

$$D_{\text{eff}} = D - \frac{2nf_{\text{s}}L_{\text{leak}}}{V_{\text{in}}}\left(2I_{\text{Lo}} - \frac{V_{\text{o}}}{L_{\text{o}}}\frac{D'}{2f_{\text{s}}}\right). \tag{29}$$

Here, D is the duty cycle of the primary voltage set by the converter controller, $n = n_{\text{s}}/n_{\text{p}}$ is the transformer turns ratio, V_{in} and V_{out} are the converter input and output voltages, respectively, f_{s} is the switching frequency, I_{Lo} is the output inductor current, L_{o} is the output inductor, and L_{leak} leak is the leakage inductance of the transformer. Small-signal transfer functions of the PSFB depend on the leakage inductance L_{leak}, the switching frequency f_{s}, perturbations of the output filter inductor current $\hat{I}_{\text{Lo}}$, the input voltage $\hat{v}_{\text{in}}$, and the primary voltage duty cycle $\hat{d}$. To accurately model the dynamic behavior of the PSFB, the contributions of all these previous parameters have to be taken into consideration. Taking into account the duty cycle modulation due to the change of output filter inductor current $\hat{d}i$ and change of the input voltage $\hat{d}v$, the total change of the effective duty $\hat{d}_{\text{eff}}$ can be given as

$$\hat{d}_{\text{eff}} = \hat{d} + \hat{d}i + \hat{d}v \tag{30}$$

for PSFB converter applications, electrolytic output capacitors are used rather than ceramic ones which might otherwise justify a negligible ESR. Thus, the ESR of the output capacitor cannot be ignored because it is responsible for a zero in the converter transfer function. the transfer function of the PWM switch PSFB converter

has been evaluated and the control-to-output transfer function is given as

$$G_{\mathrm{vd}} = \frac{nV_{\mathrm{in}}}{S^2 L_{\mathrm{o}} C_{\mathrm{o}} + s\left(\frac{L_{\mathrm{o}}}{R_{\mathrm{load}}} + R_{\mathrm{d}} C_{\mathrm{o}}\right) + \frac{R_{\mathrm{d}}}{R_{\mathrm{load}}} + 1}, \tag{31}$$

where $R_{\mathrm{d}} = 4n2f_{\mathrm{s}}L_{\mathrm{leak}}$. The term $R_{\mathrm{d}}/R_{\mathrm{load}} + 1$ in (31) is important in the dynamic analysis of the converter as it jointly takes into account the influence to leakage inductance L_{leak}, transformer turn ratio n, and load resistance R_{load}, in the control-to-output transfer function. Also using assumptions mostly referred to the typical PSFB applications discussed in the 1980s and 1990s, a range of 0—0.5 and a typical value of 0.25 are suggested for the term $R_{\mathrm{d}}/R_{\mathrm{load}}$.

6. Simulation and experimental results

The components chosen for building the prototype are given in Table 2. Four main switches are driven by PWM signals. The gate-driving signal to the auxiliary switch is generated according to the main switches signals. System is controlled by digital controller STM32F334 [20].

Table 2. Utilized components of the prototype

Components	Value
S1–S4	STW26NM60
C1–C4	150 pF
Sa	STP20NM60
Dr1–Dr4 and Da	DNA30EM2200
L	220 µF
Lr	2 µF
Co	2 µF/2400 V
Turns ratio of T and T_{aux}	1:5
Gate Driver	TLP152
Controller	STM32F334

Figure 4 shows the simulation results. It is noted that the simulated results have good agreement with the theoretical ones, which prove the accuracy of the theoretical analysis.

Experimental waveforms are depicted in Fig. 5 and Fig. 6. All switches can achieve ZCS in both turn-on and turn-off. Resonant current peak at the main switches is regulated at the required value. Some oscillations appear during the switching transitions in Fig. 5 because of the resonance caused by the parasitic capacitances of the rectifier diodes and the leakage inductance for the transformer. These parasitic elements are ignored in the theoretical analysis, leading for some observed differences between the experimental results and theoretical analysis.

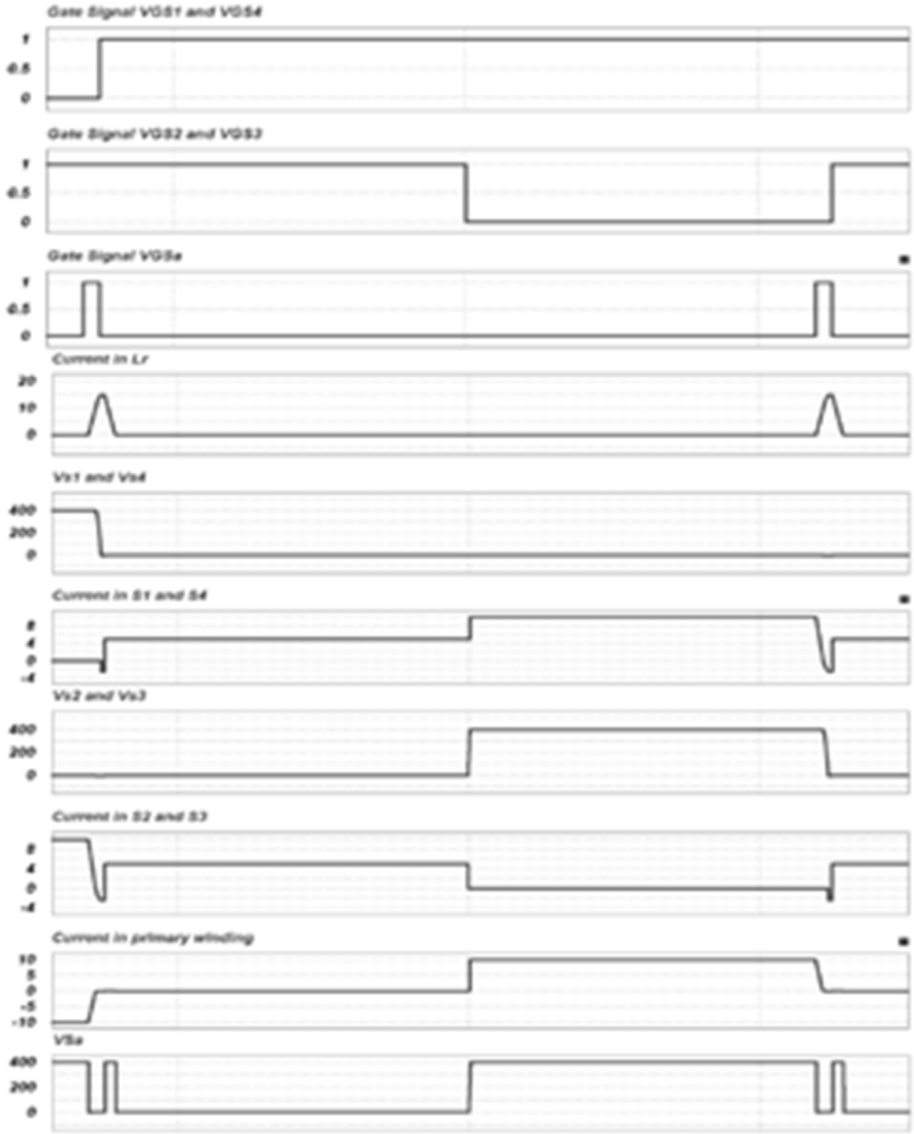

Fig. 4. Simulation results

The energy transfer efficiency comparison between the prototype and hard-switching full bridge converter operating with same components and same power is presented at Fig. 7. By using the proposed ZVS snubber, the efficiency is around 95 % at nominal load.

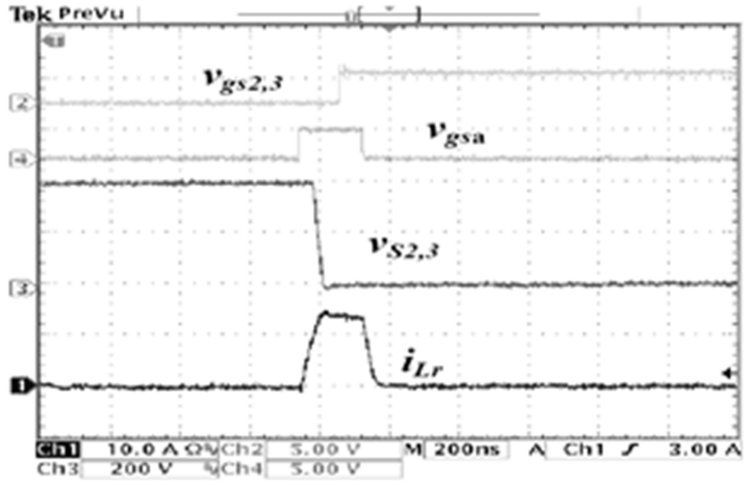

Fig. 5. Switches driving signals, resonant inductor current and voltage across S2 and S3 (i_{Lr}: 10 A/division, v_{cr}: 200 V/division, $V_{\mathrm{out}} = 2000$ V)

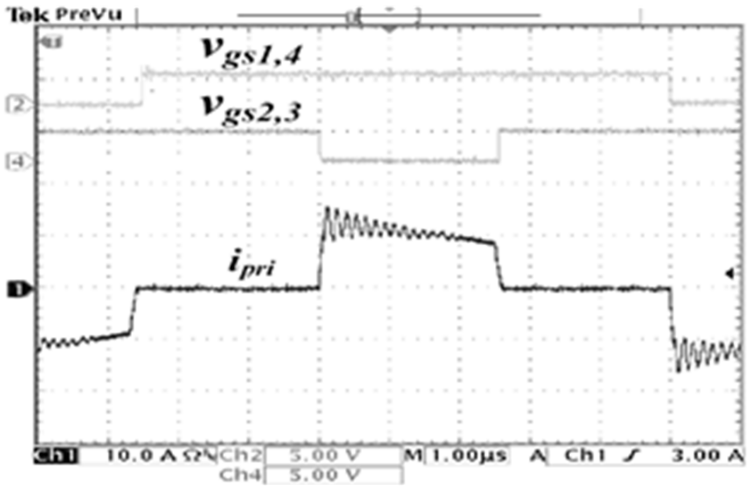

Fig. 6. Switches driving signals, and current through primary winding (i_{Lr}: 10 A/division, v_{cr}: 200 V/division, $V_{\mathrm{out}} = 2000$ V)

7. Enhanced dynamic modeling of the PSFB

7.1. Formulation of the PSFB dynamic model

The corresponding circuit for the PSFB PWM switch-based model is shown in Fig. 8. The three terminals equivalent functional block (identified by nodes a, p, c [20]) includes a three terminals PMW switch block (identified by nodes a, p, and c [21]) the equivalent losses dependent resistance R_{eq} (included between terminals c

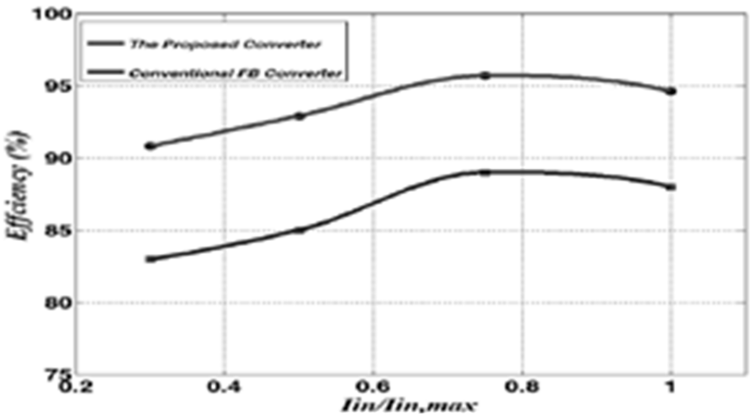

Fig. 7. Efficiency comparison

and c).

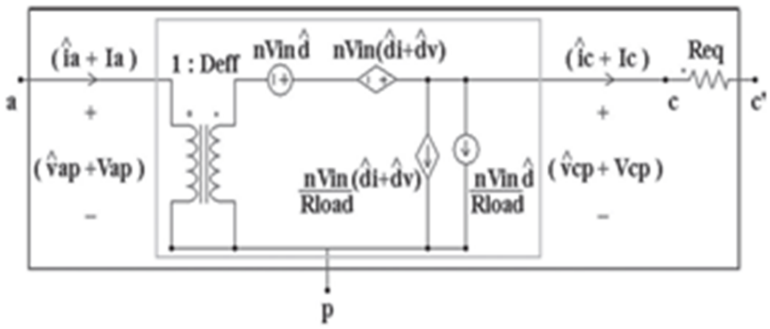

Fig. 8. Circuit model of the PWM switch for the PSFB

In particular, the equivalent resistance R_{eq} depends on the total power losses of the converter and allows the PSFB efficiency of be account within the proposed dynamic model. The circuit model to the effective duty is represented by means of a voltage-controlled source and current-controlled source.

The equations of the equivalent DC PSFB converter circuit in Fig. 9, top part, are summarized as follows:

$$I_{\mathrm{a}} = D_{\mathrm{eff}} I_{\mathrm{c}}, \quad V_{\mathrm{cp}} = D_{\mathrm{eff}} V_{\mathrm{ap}}, \quad V_{\mathrm{cp}} = R_{\mathrm{eq}} I_{\mathrm{c}} + V_{\mathrm{c'p}}\,,$$

$$P_{\mathrm{loss}} = V_{\mathrm{out}} I_{\mathrm{out}} (1-\eta)/\eta - R_{\mathrm{eq}} I_{\mathrm{out}}^2\,, \tag{32}$$

where $V_{\mathrm{ap}} = nV_{\mathrm{in}}$ and $V_{\mathrm{cp}} = V_{\mathrm{out}}$.

Solving the system equation (32) provides the DC value of duty D_{eff} and the equivalent loss-dependent lumped resistance R_{eq}. Output inductor DC series resis-

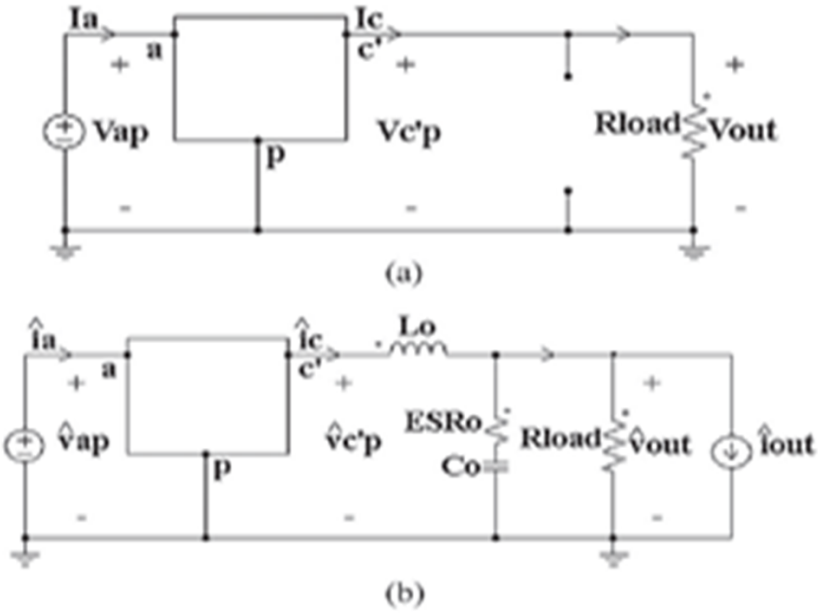

Fig. 9. top–PSFB DC equivalent model, bottom–small-signal equivalent model

tance DCR_{o} has been included in the resistance R_{eq}.

For the PSFB ac model, the equivalent AC PSFB converter circuit of Fig. 9, bottom part, is considered.

$$\hat{i}_{\mathrm{a}} = D_{\mathrm{eff}}\hat{i}_{\mathrm{c}} + \hat{d}_{\mathrm{eff}} I_{\mathrm{c}}, \quad \hat{v}_{\mathrm{cp}} = D_{\mathrm{eff}}\hat{v}_{\mathrm{ap}} + \hat{d}_{\mathrm{eff}} V_{\mathrm{ap}}\,,$$

$$\hat{v}_{\mathrm{cp}} = (R_{\mathrm{eq}} + sL_{\mathrm{o}})\hat{i}_{\mathrm{c}} + v_{\mathrm{c'p}}, \quad \hat{i}_{\mathrm{c}} = \hat{i}_{\mathrm{C0}} + \frac{\hat{v}_{\mathrm{out}}}{R_{\mathrm{load}}} + \hat{i}_{\mathrm{out}}$$

$$\hat{v}_{\mathrm{out}} = \left(\mathrm{ES}R_{\mathrm{o}} + \frac{1}{sC_0}\right)\hat{i}_{\mathrm{C0}}\,, \tag{33}$$

$$\hat{d}_{\mathrm{eff}} = \hat{d} - \frac{R_{\mathrm{d}}}{V_{\mathrm{ap}}}\hat{i}_{\mathrm{c}} + \left(I_{\mathrm{c}} - \frac{V_{\mathrm{out}}D'_{\mathrm{eff}}}{4f_{\mathrm{s}}L_0}\right)\frac{R_{\mathrm{d}}}{V_{\mathrm{ap}}^2}\hat{v}_{\mathrm{ap}}\,. \tag{34}$$

Here, $\hat{v}_{\mathrm{ap}} = n\hat{v}_{\mathrm{in}}$, $\hat{v}_{\mathrm{cp}} = \hat{v}_{\mathrm{out}}$, and $D_{\mathrm{eff}} = 1 - D'_{\mathrm{eff}}$. Using the MATLAB Symbolic Toolbox, the analytical expressions of the PSFB transfer functions have evaluated and their explicit formulations are presented in the following.

The duty-to-output transfer function Gvd represents the sensitivity of output voltage to duty-cycle variations, when input voltage and output current are locked at their steady-state values. Transfer function G_{vd} is the most important in control loop design. In voltage mode control, G_{vd} is connected to the control-to-output transfer function $G_{\mathrm{vc}} = \hat{v}_{\mathrm{out}}/\hat{v}_{\mathrm{ctr}} = \mathrm{GPWM}G_{\mathrm{vd}}$, where GPWM is the PWM modulator gain and $\hat{v}_{\mathrm{ctr}}$ is voltage error amplifier output. The PWM modulator gain converts the

voltage error amplifier output for duty cycle and is given as $\mathrm{GPWM} = 1/V_{\mathrm{pp}}$, where V_{pp} is the peak of the PWM voltage ramp signal. G_{vc} is used to design the feedback compensator and it is also easily measurable. From (33) and (34), assuming $\hat{v}_{\mathrm{in}} = 0$, $\hat{v}_{\mathrm{out}} = 0$, and solving for $\hat{v}_{\mathrm{out}}$, the transfer function G_{vd} has been evaluated and with some algebra its analytical formulation can be written as in (35). The natural frequency ωn and the damping ratio ξ are given in (36).

$$G_{\mathrm{vd}} = \frac{\hat{v}_{\mathrm{out}}}{\hat{d}} = \frac{n v_{\mathrm{in}} R_{\mathrm{load}}}{L_{\mathrm{o}} C_{\mathrm{o}} (R_{\mathrm{load}} + \mathrm{ESR}_{\mathrm{o}})} \cdot \frac{s\mathrm{ESR}_{\mathrm{o}} C_{\mathrm{o}} + 1}{s^2 + s2\omega_{\mathrm{n}}\xi + \omega_{\mathrm{n}}^2}\,, \tag{35}$$

$$\xi = \frac{\sqrt{\frac{L_{\mathrm{o}}}{C_{\mathrm{o}}}} + \sqrt{\frac{C_{\mathrm{o}}}{L_{\mathrm{o}}}} \left[(R_{\mathrm{load}} + \mathrm{ESR}_0)(R_{\mathrm{load}} + R_{\mathrm{eq}} + 4n^2 f_{\mathrm{s}} L_{\mathrm{leak}}) - R_{\mathrm{load}}^2 \right]}{2\sqrt{(R_{\mathrm{load}} + \mathrm{ESR}_0)(R_{\mathrm{load}} + R_{\mathrm{eq}} + 4n^2 f_{\mathrm{s}} L_{\mathrm{leak}})}}\,,$$

$$\omega_{\mathrm{n}} = \frac{1}{\sqrt{L_{\mathrm{o}} C_{\mathrm{o}}}} \sqrt{\frac{R_{\mathrm{load}} + R_{\mathrm{eq}} + 4n^2 f_{\mathrm{s}} L_{\mathrm{leak}}}{R_{\mathrm{load}} + \mathrm{ESR}_{\mathrm{o}}}}\,. \tag{36}$$

According to (35), the transfer function G_{vd} exhibits a second order dynamic with pair of poles, additional extra-zero that depends upon the output capacitor, and a gain related to the output filter parameters, the converter input and output voltages and the transformer turns ratio. From (36), in the bottom of the next page, it can be seen how the ESR of the output capacitor not only adds a zero to PSFB dynamic system but also impacts the damping ratio ξ, as well as the natural frequency ωn. Furthermore, the appearance of the equivalent resistance R_{eq} in the natural frequency term ωn also confirms that the resonance will change according to the PSFB losses.

The line-to-output transfer function G_{vq} represents the sensitivity of output voltage to input voltage variations, when duty cycle and output current are locked at their steady-state values. From (36) and (37), now assuming $\hat{d} = 0$, $\hat{i}_{\mathrm{out}} = 0$ and solving for $\hat{v}_{\mathrm{out}}$, the transfer function G_{vq} has been evaluated and its analytical formulation is given in (37). The DC gain of the transfer function G_{vq} depends on the voltage/current operating conditions and on the circuit parasitics, whose effect on the PSFB damping and resonance properties has already been emphasized for the G_{vd}.

Load-to-output transfer function Z_{out} represents the sensitivity of output voltage to output current variations, when duty-cycle and input voltage are locked at their steady-state values. From (33) and (34), now assuming $\hat{d} = 0$, $\hat{v}_{\mathrm{in}} = 0$ and solving for $\hat{v}_{\mathrm{out}}$, the transfer function Z_{out} has been evaluated and its analytical formulation is given in (37). According to (37), the transfer function Z_{out} has a pair of poles and two extra zeros, one depending on the ESR of the output capacitor and another depending on the output inductor, the equivalent resistance R_{eq}, the switching frequency, and the transformer parameters. Now

$$G_{\mathrm{vg}} = \frac{\hat{v}_{\mathrm{out}}}{\hat{v}_{\mathrm{in}}} = \left[n D_{\mathrm{eff}} + n^2 L_{\mathrm{leak}} \frac{V_{\mathrm{o}}}{V\mathrm{in}} \left(\frac{4 f_{\mathrm{s}}}{R_{\mathrm{load}}} - \frac{D'_{\mathrm{eff}}}{L_0} \right) \right] \times$$

$$\frac{R_{\text{load}}}{L_{\text{o}}C_{\text{o}}(R_{\text{load}}+\text{ESR}_{\text{o}})}\cdot\frac{(s\text{ESR}_{\text{o}}C_{\text{o}}+1)}{s^2+s2\omega_{\text{n}}\xi+\omega_{\text{n}}^2}\,, \tag{37}$$

$$Z_{\text{out}}=\frac{R_{\text{load}}}{L_{\text{o}}C_{\text{o}}(R_{\text{load}}+\text{ESR}_{\text{o}})}\cdot\frac{(R+4n^2f_{\text{o}}L_{\text{leak}}+sL_{\text{o}})(s\text{ESR}_{\text{o}}C_{\text{o}}+1)}{s^2+s2\omega_{\text{n}}\xi+\omega_{\text{n}}^2}\,. \tag{38}$$

7.2. Experimental verification

The following operating conditions were applied: $V_{\text{in}} = 36\,\text{V}$, $V_{\text{out}} = 14\,\text{V}$, $I_{\text{out}} = 10\,\text{A}$ and $f_{\text{s}} = 188\,\text{kHz}$. Main power devices mounted on the board are listed in Table I. All the converter open-loop transfer functions were measured using the OMICRON Lab Bode 100 vector network analyzer. In order to verify the validity of the proposed dynamic model, measurements output filter components and of the transformer were carried out and the following measured values were obtained: $C_{\text{o}} = 1354\,\mu\text{F}$, $\text{ESR}_{\text{o}} = 21.2\,\text{m}\Omega$, $L_o = 5.3\,\mu\text{FH}$, $\text{DCRo} = 35.4\,\text{m}\Omega$, and L_{leak}, see Fig. 10. PSFB board was used for the experimental measurements.

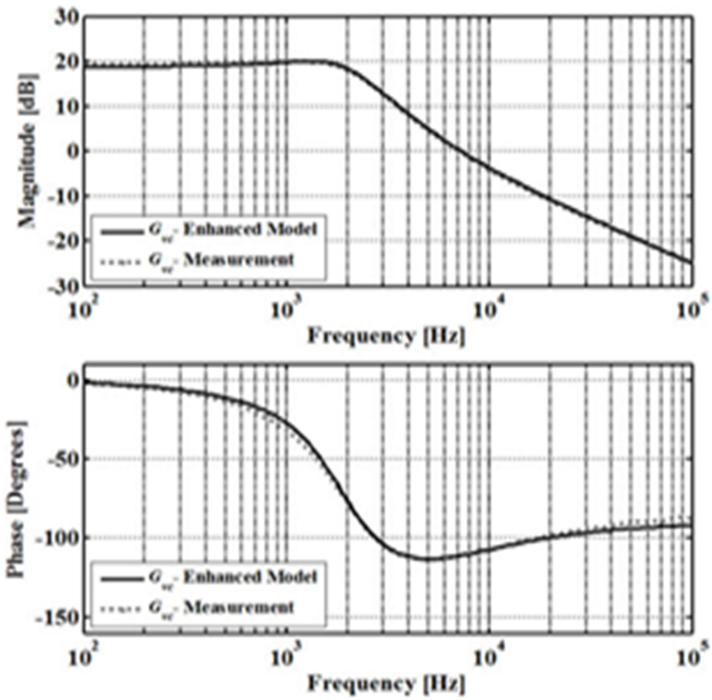

Fig. 10. Measured (dotted lines) and simulated (solid lines) control-to-output transfer function

The measured and the simulated results for the control-to output transfer function G_{vc} is shown in Fig. 4: there is excellent agreement between the experimental

result (dashed gray line) and the proposed PSFB enhanced dynamic model (black continuous line). Experimental measurements (dashed gray line) and simulated results (black continuous line) to the input-to-output transfer function G_{vg} and the load-to-output transfer function Z_{out} are shown in Figs. 11 and 12, respectively.

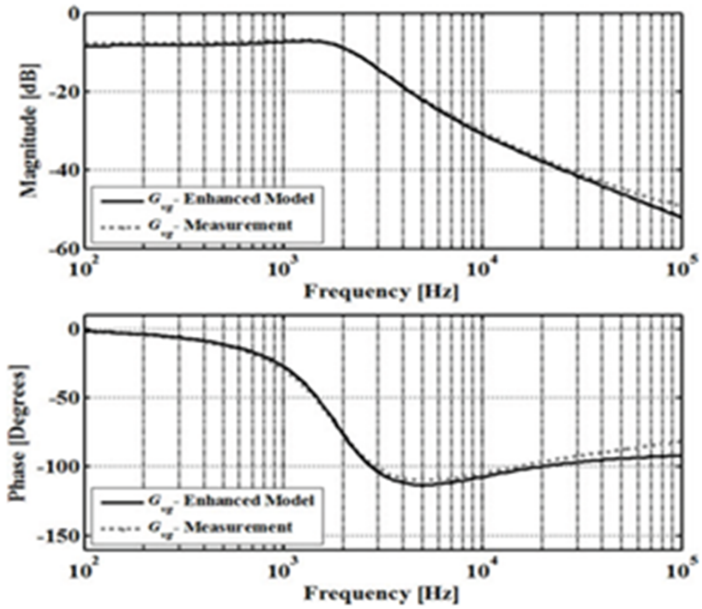

Fig. 11. Measured (dotted lines) and simulated (solid lines) input-to-output transfer function

7.3. Impact of ESL in the PSFB Dynamic Model

At higher frequencies, the agreement between the experimental results and the proposed PSFB enhanced dynamic model can be improved further to taking into account the effect of the equivalent series inductance of the output capacitor. for include the ESLo in the PSFB AC model (33e) should be replaced by

$$\hat{v}_{\mathrm{out}} = \left(\mathrm{ES}R_{\mathrm{o}} + \frac{1}{sC_{\mathrm{o}}} + s\mathrm{ES}L_{\mathrm{o}} \right) \hat{i}_{\mathrm{Co}} \,. \tag{39}$$

Using a value of $\mathrm{ESL_o} = 5\,\mathrm{nH}$, experimental and the simulated results are almost identical at higher frequencies to 1 MHz, as shown in Fig. 7. The achieved agreement once again confirms the accuracy of the proposed dynamic model.

Nevertheless, it should be noted that typically frequencies above open-loop crossover frequency are of little interest in control loop design. Model without the addition of the $\mathrm{ESL_o}$ is acceptable for most cases.

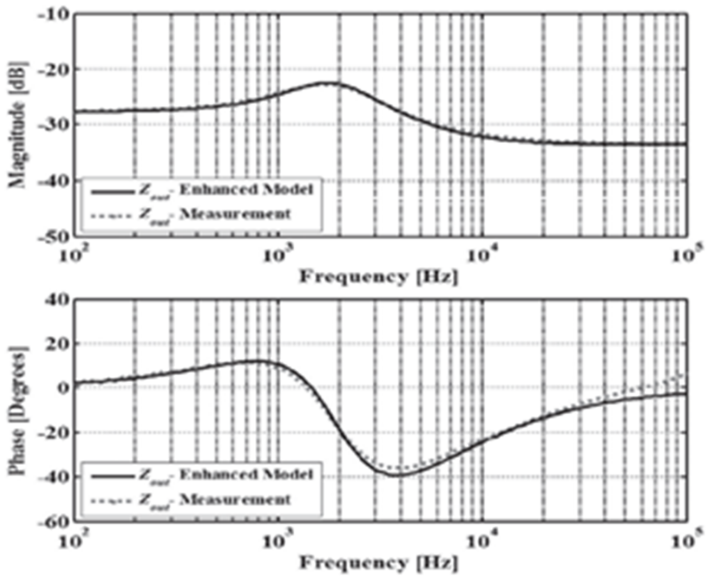

Fig. 12. Measured (dotted lines) and simulated (solid lines) load-to-output transfer function

8. Impact of the dynamic model on PSFB compensator design

The proposed dynamic model permits reliable compensator design for the PSFB, with a predictable and accurate value of the crossover frequency and acceptable amount of phase. Figure 13 shows the measured and simulated control-to-output transfer functions including $\mathrm{ESL_o}$.

The loop gain of the converter $T_\mathrm{c} = G_\mathrm{va}$, where G_va is the compensator gain to be designed based on the control-to-output transfer function G_vc. Given the design specifications mentioned in Section III, the G_vc transfer function can be calculated as derived in the same section. Clearly understand the impact to improper dynamic modeling on the closed-loop transfer functions to the PSFB, the compensator design for the aforementioned case study is discussed in the remainder of this section. The compensator has been derived based on the K-factor approach [22] by using the two following PSFB dynamic models:

1) The model proposed in this paper, labeled as the enhanced model, including the parasitic parameters and

2) The model proposed in [21], labeled as the simplified model, where $4n2f_\mathrm{s}L_\mathrm{leak}R_\mathrm{load} = 0.25$ and $\eta = 100\,\%$.

The following dynamic specifications have been adopted for the compensator design: a crossover frequency $f_\mathrm{c} = 3.5\,\mathrm{kHz}$ and a phase margin $P_\mathrm{m} = 65\,^\circ$. It should be noted that a crossover frequency of around 3–5 kHz is usually the highest achievable crossover frequency for an isolated converter using optoisolator in the

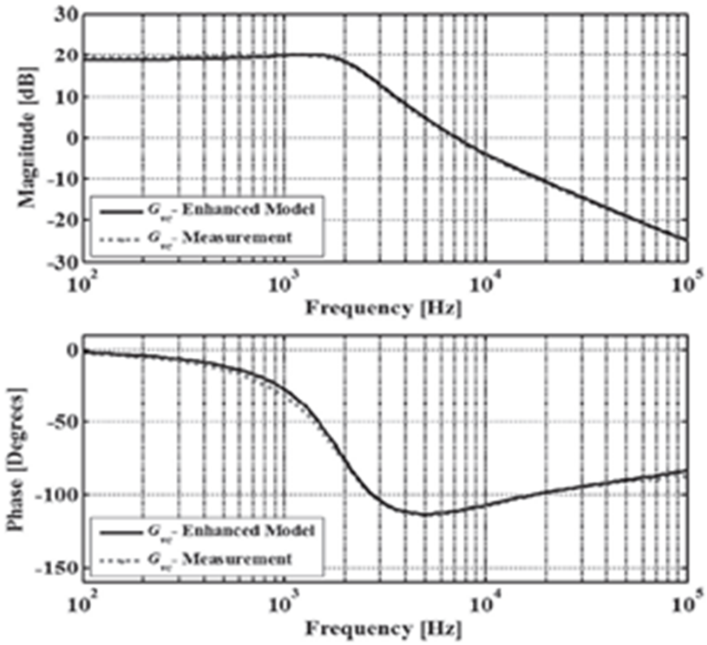

Fig. 13. Measured and simulated control-to-output transfer function including $\mathrm{ESL_o}$

control loop. Therefore, it is necessary to ensure a predictable value of f_c using the model to comply with this specification. The compensator design results obtained with the enhanced and simplified models are shown in Table 3.

Table 3. Compensator design for enhanced and simplified models

Model	Controller type	Compensator design
Enhanced model	$G_{\mathrm{va,E}} = \frac{2\pi f_{\mathrm{p1}}}{s} \frac{(1+s/2\pi f_{\mathrm{z1}})^2}{(1+s/2\pi f_{\mathrm{p2}})^2}$	$f_{\mathrm{p1}} = 347\,\mathrm{Hz}$ $f_{\mathrm{z1}} = 1.80\,\mathrm{kHz}$ $f_{\mathrm{p2}} = 6.82\,\mathrm{kHz}$
Simplified model	$G_{\mathrm{va,E}} = \frac{2\pi f_{\mathrm{p1}}}{s} \frac{(1+s/2\pi f_{\mathrm{z1}})^2}{(1+s/2\pi f_{\mathrm{p2}})^2}$	$f_{\mathrm{p1}} = 830\,\mathrm{Hz}$ $f_{\mathrm{z1}} = 1.66\,\mathrm{kHz}$ $f_{\mathrm{p2}} = 7.39\,\mathrm{kHz}$

The fulfillment of all the dynamic specifications requires a Type-III controller, labeled as G_{va}, E for the enhanced model and G_{va}, and S for the simplified model. In Fig. 14, top part, the uncompensated loop gain $T_{\mathrm{u,E}}$ (gray solid line) and the compensated loop gain $T_{\mathrm{c,E}} = T_{\mathrm{u,E}}$ and $G_{\mathrm{va,E}}$ (black solid line) are shown for the enhanced model. In Fig. 14, bottom part, the uncompensated loop gain $T_{\mathrm{u,S}}$ (gray

solid line) and the compensated loop gain $T_{c,S} = T_{u,S}\ G_{va}$ (black solid line) are shown for the simplified model. The switching frequency f_s (dotted gray lines) and resulting cross-over frequencies $f_{c,E}$, $f_{c,S}$ (vertical dashed black lines) are also shown for the two models in Fig. 15. As can be seen from Fig. 14, top part, the compensator designed using the enhanced model perfectly fits the dynamic specifications, with a crossover frequency of 3.5 kHz. The compensated loop gain $T_{u,E-S} = T_{u,E}\ G_{va}$ (dashed black lines) shown in Fig. 14, bottom part, can be analyzed to understand what happens if compensator designed with the simplified model $G_{va,S}$ is used to control the real converter with losses.

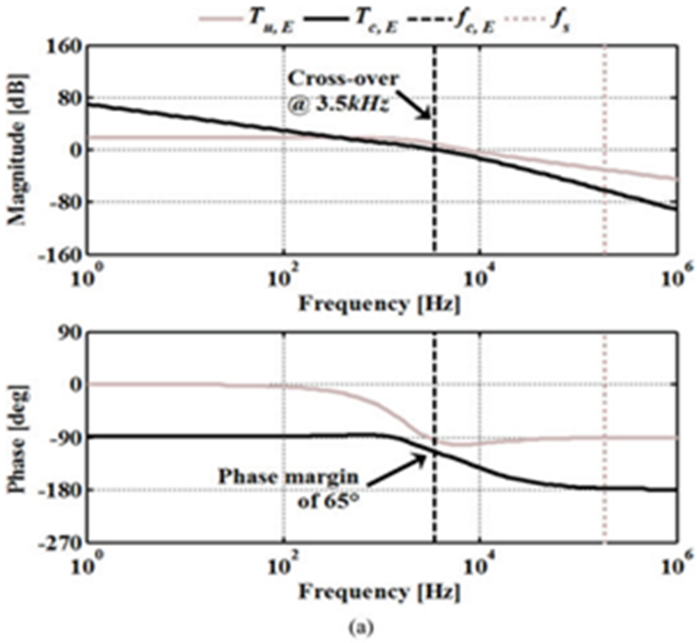

Fig. 14. Uncompensated and compensated loop gain transfer functions for: top–enhanced and bottom–simplified models

9. Conclusion

A new ZVS current-driven full-bridge converter has been presented. A simple snubber is inserted in the primary side. It realizes soft-switching for the main switches. These advantages that are not normally present in ZVS solutions mitigate the disadvantage of having a hard-switching turn-on of the snubber switch. As result to the above advantages of the proposed ZVS solution, the measured efficiency of the prototype is 95 % at rated load and 100 kHz switching frequency which is 6 % higher than the hard switching one without the auxiliary switch. Also a new model for the small-signal behavior to the PSFB converter has been presented in this paper. The global effect of circuit parasitics and efficiency has been analyzed,

by means of a compact behavioral model, allowing the evaluation of the converter open-loop transfer functions. Experimental verifications validate the proposed behavioral model. The influence of the parasitics and efficiency on the compensator design has also been investigated. The main differences between the compensated loop gain transfer functions for the proposed enhanced model and the pre-existing simplified model have been discussed. Examples highlight the impact of appropriate dynamic modeling of the PSFB on the performances of the controller.

The enhanced model to the PSFB converter presented in this paper allows for a stable, reliable, and predictable controller to be designed meeting the crossover frequency and phase margin requirements.

References

[1] I. Lee, G. Moon: *Analysis and design of phase-shifted dual h-bridge converter with a wide ZVS range and reduced output filter.* IEEE Transactions on Industrial Electronics *60* (2013), No. 10, 4415–4426.

[2] J. Zhang, H. Wu, X. Qin, Y. Xing: *PWM plus secondary-side phase-shift controlled soft-switching full-bridge three-port converter for renewable power systems.* IEEE Transactions on Industrial Electronics *62* (2015), No. 11, 7061–7072.

[3] Z. Yin, M. Chen, K. Li, A. Ioinovici: *A new ZCS PWM full-bridge converter of buck-type for applications with very high input voltage.* Annual Conference of the IEEE Industrial Electronics Society, 9-12 November 2015, Yokohama, Japan, Proceedings IECON (2015), 1495–1500.

[4] L. Zhu: *A novel soft-commutating isolated boost full-bridge ZVS-PWM DC/DC converter for bidirectional high power applications.* IEEE Transactions on Power Electronics *21* (2006), No. 2, 422–429.

[5] E. Adib, H. Farzanehfard: *Zero-voltage transition current-fed fullbridge PWM converter.* IEEE Transactions on Power Electronics *24* (2009), No. 4, 1041–1047.

[6] U. R. Prasanna, A. K. Rathore: *Extended range ZVS active-clamped currentfed full-bridge isolated DC/DC converter for fuel cell applications: Analysis, design, and experimental results.* IEEE Transactions on Industrial Electronics *60* (2013), No. 7, 2661–2672.

[7] U. R. Prasanna, A. K. Rathore: *Small-signal modeling of activeclamped ZVS current-fed full-bridge isolated DC/DC converter and control system implementation using PSoC.* IEEE Transactions on Industrial Electronics *61* (2014), No. 3, 1253–1261.

[8] S. R. Sanders, J. M. Noworolski, X. Z. Liu, G. C. Verghese: *Generalized averaging method for power conversion circuits.* IEEE Transactions on Power Electronics *6* (1991), No. 2, 251–259.

[9] V. Vorperian: *Simplified analysis of PWM converters using model of PWM switch. Continuous conduction mode.* IEEE Transactions on Aerospace and Electronic Systems *26* (1990), No. 3, 490–496.

[10] J. A. Sabate, V. Vlatkovic, R. B. Ridley, F. Lee, H. B. Cho: *Design considerations for high-voltage high-power full-bridge zero-voltages witched PWM converter.* Annual Proceedings on Applied Power Electronics Conference and Exposition, 11–16 March 1990, Los Angeles, CA, USA, Proceedings APEC (1990), 275–284.

[11] V. Vlatkovic, J. A. Sabate, R. B. Ridley, F. C. Lee, B. H. Cho: *Small-signal analysis of the phase-shifted PWM converter.* IEEE Transactions on Power Electronics *27* (1992), No. 1, 128–135.

[12] M. J. Schutten, D. A. Torrey: *Improved small-signal analysis for the phase-shifted PWM power converter.* IEEE Transactions on Power Electronics *18* (2003), No. 2, 659–669.

[13] K. M. Cho, Y. D. Kim, I H. Cho, G. W. Moon: *Transformer integrated with additional resonant inductor for phase-shift full-bridge converter with primary clamping diodes.* IEEE Transactions on Power Electronics *27* (2012), No. 5, 2405–2414.

[14] Y. D. Kim, K. M. Cho, D. Y. Kim, G. W. Moon: *Wide-range ZVS phase-shift full-bridge converter with reduced conduction loss caused by circulating current.* IEEE Transactions on Power Electronics *28* (2013), No. 7, 3308–3316.

[15] S. Shekhawat, M. Rinehimer, B. Brockway: *FCS fast body diode MOSFET for phase shifted ZVS PWM full bridge DC/DC converter.* Fairchild Semiconductor Corporation AN-7536, San Jose, CA, USA (2011).

[16] F. di Domenico, R. Mente: *ZVS phase shift full bridge: CFD2 Optimized design.* Infineon Technilogies AN-2013/03, Villach, Austria (2013).

[17] A. Hari: *Using a phase-shifted full-bridge topology in small form factor power converters.* National Semiconductor SNVA-610, Lewisville, TX, USA (2011).

[18] J. Shi, J. Luo, X. He: *Common-duty-ratio control of input-series output-parallel connected phase-shift full-bridge DC/DC converter modules.* IEEE Transactions on Power Electronics *26* (2011), No. 11, 3318–3329.

[19] H. Nene: *Digital control of a bi-directional DC/DC converter for automotive applications.* Twenty-Eighth Annual IEEE Applied Power Electronics Conference and Exposition (APEC), 17–21 March 2013, Long Beach, CA, USA, Proceedings APEC (2013), 1360–1365.

[20] G. S. Ho, C. C. Lin, S. H. Hsu, Y. Y. Tzou: *SoPC based digital current-mode control of full-bridge phase-shifted DC/DC converters with fast dynamic responses.* IEEE International Conference on Power Electronics and Drive Systems, 22–25 April 2013, Kitakyushu, Japan, Proceedings PEDS (2013), 113–118.

[21] M. Hallworth, B. A. Potter, S. A. Shirsavar: *Analytical calculation of resonant inductance for zero voltage switching in phase-shifted full-bridge converters.* IET Power Electronics *6* (2013), No. 3, 523–534.

Received October 12, 2017